Master of Science Thesis

^{90}Y-Scintigraphy of small animals: A study of imaging parameters.

Melinda Joo

Supervisors:
Michael Ljungberg and Cecilia Hindorf

Department of Medical Radiation Physics
The Jubileum Institute
Lund University

2003

LUJI-RADFYS-EX-4/2003

TABLE OF CONTENTS

Populärvetenskapligt beskrivning

På grund av sin höga energi, 2.28 MeV, och den korta halveringstiden, 64.1 timmar, har Yttrium-90, som är en β–emitterare, visat sig vara en lovande radionuklid inom cancerbehandling genom radionuklidterapi. β–partiklarna är i sig inte lämpliga som bas för bildgenerering över var i objektet aktiviteten är fördelad men man kan istället utnyttja de sekundära bromsstrålningsfotonerna för en avbildning med en gammakamera. Bromsstrålningsfotonerna har dock ett brett energispektrum, från noll till β-partikelns maximala energi, vilket gör att valet av kollimator och energifönsterinställningar på gammakameran inte är triviala.

Avsikten med detta examensarbete var att undersöka vilka gammakamerainställningar ger bäst bild, då man utnyttjar bromsstrålningen från Y-90 för att avbilda aktivitetsfördelningen i små djur. Fotonerna som utgör grunden för bildgenereringen kan vara primära eller spridda i objektet. För vår del är endast de primära fotonerna intressanta eftersom de spridda försämrar bildkontrasten. Dessa kan aldrig dock inte till 100% särskiljas från de spridda fotonerna i experimentella mätningar. Med hjälp av Monte Carlo beräkningar kan man genom ett datorprogram följa varje foton från dess ursprung tills att den registreras och på så sätt dela upp bilden i dessa komponenter.

I experimentella mätningar använde jag en vattenfantom av en råttas storlek i vilken en tumör simulerades med hjälp av en sfär fylld med Y-90. Bilder togs med gammakamera för olika kollimatorer och olika energifönsterinställningar. Vid val av kollimator handlar det ofta om en kompromiss mellan känslighet och upplösning. En lågenergikollimator har bättre känslighet men en sämre rumsupplösning, medan det är tvärtom vid en högenergikollimator eftersom septumpenetrationen minskar på grund av tjockare septum (hålvägg).

Resultaten visade bäst känslighet med lågenergi kollimatorn och där denna ökade med bredare energifönster för samma kollimator. Den höga känsligheten medför en försämring av den spatiella upplösningen. Förhållandet mellan primära och spridda fotoner var nästan oberoende av energifönsterbredd, men drygt tre gånger bättre för högenergikollimatorn än för lågenergikollimatorn. Våra experimentella mätningar visar att man får bäst bildkvalité med högenergikollimator och bredast möjlig energifönster (99 % centrerad kring 170 keV).

Programmet som används vid Monte Carlo beräkningar kan särskilja tre typer av händelser: a) händelser från geometriskt kollimerade fotoner som passerar hålen utan att växelverka i kollimatorn, b) händelser från fotoner som passerar genom två eller flera hål eftersom de penetrerar septumväggen och c) händelser från fotoner som sprids i kollimatorns hålväggar. Kunskapen om dessa förhållande kan vara väldigt viktig då man utvecklar korrektionsmetoder för spridning, attenuering och septum penetration.

Abstract

Yttrium-90 is a pure β-emitting radionuclide with a high energy (Emax = 2.28 MeV) and a short half-life (T½ = 64.1 h). It has shown to be a promising isotope to use in radio-immunotherapy. In the absence of direct photon emission scintillation camera imaging can be

obtained by acquiring events from bremsstrahlung photons created at or near the decay site of the radionuclide. It is, however, not evident how the energy window has to be defined, because the photon energy spectrum from the interacting β-particles extends from zero to the maximum energy of the β-particle. The aim of this master's work was to examine the imaging parameters of the gamma camera (energy window, collimator) to achieve information in order to determine the optimum conditions for bremsstrahlung imaging. Methods: A Siemens DIACAM scintillation camera and a water phantom simulating a rat were used for the experimental studies. Spheres, filled with 90Y, simulated tumours. Three collimators denoted LEAP (Low-Energy All Purpose), HE (High-Energy) and UHE (Ultra High Energy) were investigated for various settings of the energy window. The system sensitivity [cps/MBq] and the primary-to-total radiation ratio were compared for the three collimators and the different energy window settings. In addition, Monte Carlo simulations using the SIMIND code were made to demonstrate how the image quality degrades as function of physical parameters. The simulations were setup in such a way that the components in the images from geometrical penetrating and scatter events were separated. Results: The LEAP collimator showed the highest sensitivity as expected, but also the lowest image quality because of the septum penetration. The UHE collimator has, generally, lower sensitivity and lower ratio of primary-to-total radiation than the LEAP collimator but the septal penetration was less than the LEGP. The HE collimator with an energy window between 86-254 keV was selected as optimal acquisition setting with consideration of both the sensitivity and primary-to-total ratio. The lower limit of 86 keV for the energy windows was chosen to eliminate the characteristic K X-ray photons, with energies 74.97 keV (46.2%), 72.81 keV (27.7%), 84.94 keV (10.7%) and 84.45 keV (5.58%) [1]. Results from the simulations also showed that a large fraction of the recorded events when using the LEAP collimator originates from photons that have penetrated the septal walls. As the energy window decreased the ratio primary-to-total increased which means that fewer scattering and penetrating events are registered. The simulations also show that the penetration is a significant problem for the LEAP collimator, while the UHE collimator shows the smallest penetration fraction.

Background

The administration of β-emitting radionuclides for radionuclide therapy has been used for decades. In the early nineties, radio-labeled antibodies were accepted in cancer therapy. A number of β-emitting radionuclides is available, i.e. ^{32}P, ^{89}Sr, ^{131}I and ^{90}Y. Yttrium-90 has been shown to be a promising isotope in therapy with labelled antibodies because of the long path-length of the particles. An expected result of the high energy (E_{max} = 2.28 MeV) and the short half time ($T_{½}$ = 64.1 h) is a large absorbed dose to the tumour without transferring too much energy outside its boundaries. In most cases the energy of the β-particles are not large enough for a direct detection since 90% of the energy is deposited within 5.2 mm [2]. The absence of photons in the decay of ^{90}Y has therefore led to the use of ^{111}In for pre-therapy imaging. Indium-111 is a radionuclide with chemical properties comparable to ^{90}Y with

emission of two photons in cascade of energies 171 and 245 keV that is suitable for scintillation camera imaging [1]. Since the chemical properties are not identical, it has become evident that the ^{111}In activity distribution may not predict the ^{90}Y activity distribution behaviour *in vivo* completely. This problem can be eliminated using the indirect photon emission, caused by the slowing-down process of the β-particles from ^{90}Y, but these bremsstrahlung photons have a broad energy spectrum of energies so the choice of collimator and energy window is not trivial.

Bremsstrahlung radiation

When fast electrons interact with matter, they undergo various scatterings by collision processes. One such interaction type is the inelastic scattering of electrons with the nucleus. In this interaction type, the electron undergo a significant angular deflection relative its initial path with a significant loss of kinetic energy. Because of the energy conservation law, slowing-down charged particles must transfer energy to other particles or emit the excess of energy as electromagnetic radiation. Such a radiation is called bremsstrahlung [3-5]. The theoretical expression that describes the specific energy loss per unit distance, $\left(\frac{dE}{dx}\right)$, can be derived from quantum mechanical calculations. This was firstly performed in 1930 by Hans Bethe. The electrons transfer energy by either collisions, $\left(\frac{dE}{dx}\right)_c$, which results in ionisation or excitation, or as irradiative losses, $\left(\frac{dE}{dx}\right)_r$ that take the form of bremsstrahlung emission. The irradiative losses can emanate from any position along the electron track and this is the reason why the bremsstrahlung energy spectrum is a continuum of photon energies between zero and the maximum electron energy.

The linear specific energy loss trough radiation, $\left(\frac{dE}{dx}\right)_r$, is given as follow:

$$\left(\frac{dE}{dx}\right)_r = \left(\frac{e^2}{4\pi\varepsilon_0}\right)^2 \frac{Z^2 N_A (T+mc^2)\rho}{137 m^2 c^4 A}\left[4\ln\frac{2\left(T+mc^2\right)}{mc^2} - \frac{4}{3}\right] \qquad (1.1)$$

where Z, A and ρ are the atomic number, the atomic weight and the density of the attenuating material. The parameters, m and T, are the electron rest mass and its kinetic energy, respectively and e, ε_0, N_A and c are the charge of electron, permittivity constant, Avogadro's number and the speed of light in vacuum, respectively. Equation 1.1 shows that the irradiative losses are most important for high electron energies and for materials with large atomic numbers. The total energy loss for electrons is the sum of the collision and irradiative losses:

$$\frac{dE}{dx} = \left(\frac{dE}{dx}\right)_c + \left(\frac{dE}{dx}\right)_r \tag{1.2}$$

The ratio of the specific energy losses is given approximately by equation (1.3):

$$\frac{(dE/dx)_r}{(dE/dx)_c} \approx \frac{(E + mc^2)\cdot Z}{1600 \cdot mc^2} \approx \frac{E \cdot Z}{800} \tag{1.3}$$

An approximation of radiation losses for β-particles which results in bremsstrahlung production is given by:

$$\textit{Percentage radiation losses} \approx \left(ZE_\beta^{\max} / 3000\right) \times 100\,\% \tag{1.4}$$

where $E_\beta^{\max}$ is the maximum energy of the β particle in MeV. The fraction of the electron energy that is converted into bremsstrahlung photons increases as the electron energy is increased and reaches large values for absorbing materials of high atomic numbers. When these fast electrons pass trough an absorber, not only bremsstrahlung photons with a broad energy spectrum are produced, but also characteristic X-ray emission lines. These lines are over-layered on the continuous bremsstrahlung spectrum.

The scintillation camera

The scintillation camera is the most commonly used imaging system in nuclear medicine today and can be considered as a position-sensitive scintillation detector [6-8]. The principal scintillation camera was invented in 1956-57 by Hal O. Anger (a common name of the camera is therefore the Anger camera). The basic components of the scintillation camera (*Fig. 1.1*) are (a) a collimator, (b) a large-area thallium-activated sodium-iodide (NaI(Tl)) crystal, (c) a light-guide for optically coupling of the crystal to a large number of photo-multipliers tubes (PMT) and (d) electronics for position encoding and pulse-height analysis. Ideally, only the photons, emitted from a radioactive source in a direction within the angle of incidence to the collimator, will pass trough the collimator and be projected onto the crystal surface. When the photons interacts in the NaI(Tl) crystal, the atoms will be excited and subsequently this excitation will lead to emission of scintillation light that is detected and enhanced by the PM tubes. The PM tubes are mostly hexagonal in shape that allows them to be closely packed.

There is a linear relationship between the intensity of the emitted scintillation light and the imparted photon energy, which means that the final electronic signal is proportional to the absorbed photon energy. The formation of a spatial coordinate of the interaction site is made by the contribution of light detection from all of the PM tubes by calculating the centroid of

the signals from each PM tube. In order to avoid a position that depends on the absorbed energy, the calculation of the final X- and Y signal are normalized by the measured energy, Z. To minimize the losses of the light in the transport between the crystal and the PM tubes, a light guide is often used that has the refractive index close to the one of the NaI(Tl) crystal. These components are also optically coupled to further avoid light refraction. The design of he light-guide also minimizes the variation in the light collection efficiency between PM tubes, which improve the uniformity of the camera.

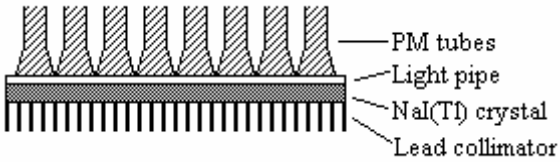

Figure 1.1 - The basic elements of a scintillation camera head**.**

The collimator defines (a) the geometrical Field-Of-View (FOV) of the camera, (b) the spatial resolution and (c) the system sensitivity of the system. There exists an inverse relation between the spatial resolution and the sensitivity for parallel-hole collimators. Thicker collimator (longer holes) means a better spatial resolution but the sensitivity will decrease since fewer photons will be able to pass the hole geometrically. Therefore, one often uses a range of collimators to achieve the optimal compromise between the spatial resolution and the sensitivity for a particular investigation. The geometrical resolution of a collimator can be increased by increasing the length of the holes but also reducing the diameter of the hole. The system resolution also depends on maintaining a close distance between the patient (source) and the collimator surface.

Most modern cameras have a large rectangular area (up to 50 cm) with a thin (6-12 mm) NaI(Tl) crystal of optimal imaging characteristic for $^{99}Tc^{m}$ imaging. NaI(Tl) yields a high light output and the crystal is highly transparent to its own light emission. NaI(Tl) crystals are sealed in a thin aluminium cover since they are both hygroscopic and fragile. A thick lead-shield (1-2 cm) surrounds the scintillation crystal and electronics to reduce the detection of external radiation from outside the collimator field-of-view.

The system sensitivity is determined by the geometrical efficiency of the collimator times the photo-peak detection efficiency of the crystal. The intrinsic spatial resolution (R_i) of the gamma camera usually is defined as FWHM and is typically 3-4 mm for 140 keV photons. When this parameter is combined with the geometrical spatial resolution of the collimator (R_c), the result provides the system spatial resolution (R_s) or:

$$R_s = \sqrt{\left(R_i^2 + R_c^2\right)} \tag{1.5}$$

For a parallel-hole collimator, the collimator spatial resolution can be expressed as:

$$R_c \approx \frac{d(L+z)}{L} \tag{1.6}$$

where L and d are the hole length and diameter, respectively, and z is the source-to-collimator distance.

Previous studies of bremsstrahlung imaging

So far, no work has been published where the settings for the gamma camera imaging small animals with ^{90}Y have been investigated. Dillehay *et al.* [9] presented a study of the use of bremsstrahlung radiation to monitor the activity distribution of ^{90}Y-labelled antibodies in nude mice with subcutaneous tumours implanted and grown in the upper thigh. The mice were imaged using a 2 cm-diameter lead collimator and a 100-200 keV energy window was here used to acquire photons transmitted through a plastic β-particle absorber. For tumours with a mass larger than 0.14 g, the authors found a good correlation between the activity measurement, based on the *in vivo* bremsstrahlung, and the activity in the tumours as measured in a calibrated well-counter.

Clarke *et al.* [10] published a method for determination of the effective attenuation coefficient for ^{32}P imaging. This radionuclide emits β-particles with a maximum energy close to the emission from ^{90}Y (1.71 MeV as compared to 2.28 MeV for ^{90}Y). A high-energy collimator was here used combined with a wide energy window in order to increase the sensitivity. Images were then filtered by a Wiener filter to partly compensate for image noise. The measurements were performed in a water phantom with a cylindrical shape as an idealized scattering medium and isolated spherical sources. The selected energy window (57-285 keV) was a combination of a 50% energy window centred at 76 keV and a 99% energy window centred at 190 keV.

Additional work with the bremsstrahlung imaging from ^{32}P was published by JA Siegel *et al* [11]. In this work phantom studies were performed to optimise the bremsstrahlung energy window setting to improve both resolution and contrast as well as to validate volumetric analysis of the reconstructed SPECT slices. A medium energy collimator and a 100 keV ± 25% energy window were found to be the optimal acquisition settings. Both planar and SPECT imaging in 116 patients were performed. All the images were of high quality and permitted visualisation of the activity distribution of ^{32}P. The injection volume of the ^{32}P determined by SPECT correlated very well with the anatomic tumour volume determined by CT.

Shen *et al,* [12] reported results from a systematic, empirical evaluation of the choice of collimator, energy window setting and attenuation correction for quantitative imaging of a body phantom. The optimal imaging settings were found to be the use of a medium-energy collimator and an energy window in the range from 55 keV to 285 keV. Shen *et al.* [13] have

also published quantitative methods for bremsstrahlung imaging of ^{90}Y sources. This study also describes the use of Wiener filtering to compensation contribution in the image due to septal penetration and scattering in the object while suppressing image noise. The conjugate geometric mean method (GM) combined with effective point source (EPS) methods was used for activity quantification. An abdominal phantom was prepared with ^{90}Y located in the liver, spleen, various tumours and background volumes in concentrations that were similar to those observed in real patient studies. Based on earlier experiments, a medium-energy collimator and a broad energy window (55-285 keV) were selected as a practical compromise between sensitivity and spatial resolution requirements for clinical applications.

Problems in scintigraphy using bremsstrahlung

When a scintillation camera is used for imaging of radionuclides that emits single-photons, the energy window is generally centred over the photo-peak and the photon energy determines the choice of the collimator. In the case of bremsstrahlung imaging, a distinct photo-peak in the energy spectrum is not present. Instead, a broad spectrum of energy absorptions ranging from zero to the maximum β-energy is registered. The energy window setting is therefore not trivial, nor is the choice of collimator.

The bremsstrahlung production from β-particle interaction in low-Z material is a low-probability event. The sensitivity of bremsstrahlung imaging will therefore be very small since less than 1% of the kinetic energy of the β-particle is emitted as bremsstrahlung radiation [5]. This possesses a limitation in the expected image quality. To increase the counting statistics, a large energy window can be used but this can result in a degradation of the spatial resolution, mainly due to detection of scattered radiation. From the experimental measurements it is impossible to distinguish the history of the radiation, i.e. is the registered photon a primary bremsstrahlung photon or has it been scattered one or several times?

It is also difficult to determine if the photon has been scattered within the phantom or from an interaction in the collimator. The low-energy collimator generally provides a higher sensitivity and a lower spatial resolution as compared to the high-energy collimator since the high-energy collimator reduces the septal penetration with thicker septa. For the same diameter with increased length of the holes, the spatial resolution improves because only the photons impinging within the acceptance angle of the holes reaches the crystal. The collimator efficiency degenerates of the same reason. When the photon energies are high enough to penetrate the septum, the spatial resolution becomes poorer. The choice of energy window and collimator with bremsstrahlung imaging is therefore a compromise between sensitivity and spatial resolution.

Aims with this work

Experimental studies in animal models are very important in radionuclide therapy research and the most used are the rat and the mice. The research contributes to the understanding of the mechanisms and hence the development of better therapy methods. Computer simulations and *in vitro* tests using cells and tissues are often used as alternative methods to animal experiments. These methods can, however, not replace the animal tests completely because the complexity and variety in a biological system can not be entirely simulated.

The purpose of this work was to investigate the collimator selection and the energy window settings when using ^{90}Y-bremsstrahlung for imaging activity distribution with a scintillation camera in a small animal model. In this investigation, a water phantom comparable in size with a rat was used where a sphere filled with ^{90}Y activity simulated a tumour in the rat. The bremsstrahlung photons, which build up the images, can be either primary (photons not interacted within the phantom) or scattered in the phantom before reaching the collimator. In the image evaluations and as input for the absorbed dose calculations, only primary photons are of interest but the main problem is that they never can be distinguished from the scattered photons. For better understanding of the imaging characteristics in these situations, Monte Carlo simulations were made.

Material and methods

The scintillation camera

The scintillation camera [14], used in this study, is a Siemens DIACAM multi-purpose camera system designed for both SPECT and planar acquisition (Siemens Medical System, Chicago, IL). The camera is of the Anger-type with a single head and a large rectangular detector. A schematic image of the camera is shown in Figure 2.1 and some of the camera parameters are given in Table 2.1.

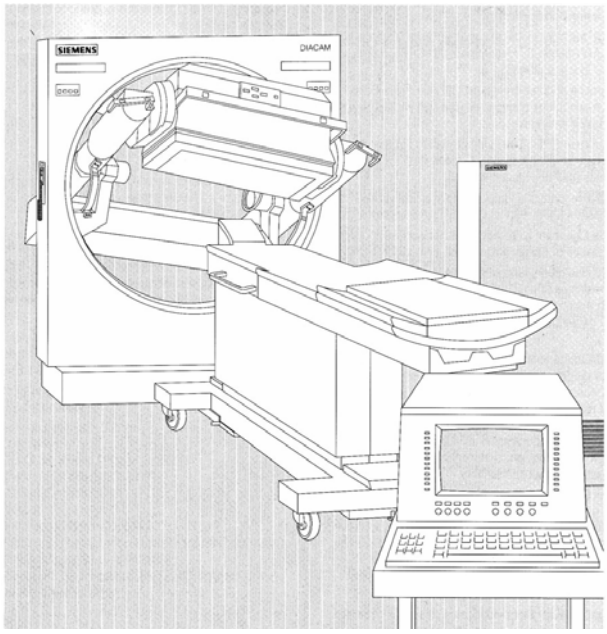

Figure 2.1 - The gamma camera system, DIACAM.

Table 2.1: Detector data.

Field of view	53.3 cm × 38.7 cm
Crystal	NaI(Tl)
Size	59.1 cm × 44.5 cm
Thickness	0.95 cm
Photo multiplier tubes	
Total number	59
Type	Bialkali, high-efficiency
Arrangement	Hexagonal
Detector shielding material	Pb
Back (top)	1.58 cm
Sides	From 1.42 cm to 1.78 cm

Depending on the energy on the photons from the radionuclide, different collimators are used and the energy window is usually set around the photo peak. The data for the collimators used in this study are presented in Table 2.2:

Table 2.2: Collimator data.

Code	**Diam** [cm]	**Septa** [cm]	**Length** [cm]	**Hole Shape**	**Comments**
LEAP	0.143	0.020	2.360	Hex	Low-Energy All Purpose
HE	0.406	0.200	5.970	Hex	High Energy Parallel

UHE	0.340	0.250	7.500	Hex	Ultra High Energy
ME	0.294	0.114	4.060	Hex	Medium Energy*

***** = This collimator was not available for experimental measurements by the data used in the Monte Carlo simulations

Because of the absence of one principal photon energy in bremsstrahlung imaging, different energy window settings have been investigated. Firstly, a study where a 15% energy window was centred at different energies ranging from 90 keV to 430 keV was made to investigate different parts of the bremsstrahlung spectrum. Secondly, measurements were performed with different width of a energy window centred at the 170 keV base line. Thirdly, measurements were made with the widest energy window available on the system (99%) centred at different energy base lines. Such a wide energy window centred at 150 keV and 290 keV corresponds to an energy window at 76 – 224 keV and 146 – 433 keV, respectively.

The water phantom

The water phantom we used for the measurements approximates the dimension of a rat. A sphere filled with ^{90}Y was placed inside the water phantom to simulate a tumour. Fig. *2.2* and table *2.3* describe the geometry of all measurements. No background activity was added. In Table 2.3 are given data for the spheres that have been imaged.

Figure 2.2 - The gamma camera and the water phantom; the measurements disposition.

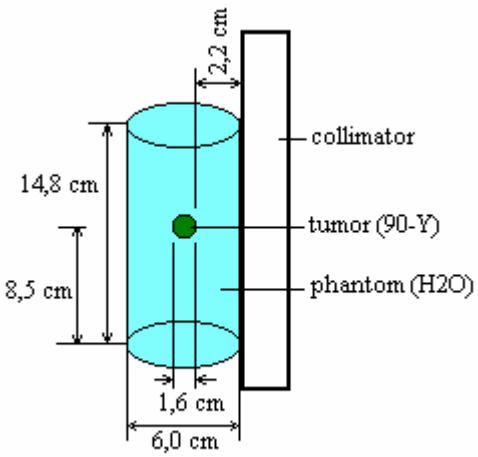

Figure 2.3 - The measurement geometry: water phantom and collimator.

Table 2.3:

The dimensions of the phantom and the tumour.

Parameters	Dimensions [cm]	Mass [g]

Phantom		420
x1 (radius)	3.00	
y1 (radius)	3.00	
z1 (length)	14.8	
Tumour		2.25
x1(radius)	0.813	
y1(radius)	0.813	
z1(radius)	0.813	
x_0	0.000	
y_0	0.000	
z_0	8.500	

The measurements in air

The sphere with the activity was freely suspended in air at the same distance to the collimator as in the case with the water phantom. The size of the sphere was identical in both measurements.

Monte Carlo calculations

Experimental measurement does not always provide all information of how an image degrades in quality because of physical parameters. To provide information about the whole process, mathematical simulations can be very useful. If an accurate model of the imaging system can be constructed then parameters otherwise 'hidden' in the pulse height distribution creating the image can be obtained. An example of such a parameter is the scatter-to-total parameter (i.e. the fraction of events in the images that comes from photons that has been scattered in the object). Ideally, these events should be discriminated because of the use of a off-setting of an energy window but since the NaI(Tl) crystal has a limited energy resolution, some of these photons still will be detected within an energy window. It is then impossible to distinguish between these events but knowledge of the amount and spatial distribution of these unwanted events are important when working with correction methods. The Monte Carlo method provides such a possibility. The method is based on sampling the random walk of the photon and selecting path length, interaction types by uniform random number. Since all details in the calculation chain in known, the separation of primary and scatter events to separate images is a straight forward process.

The program used in this work is the SIMIND code, developed at our laboratory [15]. Included in this code is a routine, developed by deVries [16] that allows simulation of photon interaction in the collimator. Three types of events can be separated a) events from geometrical collimated photons passing through the hole without interacting in the septum walls, b) events from penetrating photons that passes through one or more septum walls and c) events from photons that in some instance of its way through the collimator have been

scattered in the collimator. Ideally, only the geometrical collimated photons should be detected since these provide the best spatial information of the apparent decay location. Penetrating photons and photons scattered in the collimator degrade the spatial resolution but also limit the ability to quantify the activity since the sensitivity for a parallel-hole collimator system when including these events will not be independent on the source-collimator distance (assuming no attenuation is present).

In this work, we have studies the origin of the events in six energy windows. The simulations were made in such a way that the components in the images from geometrical, penetrating and scatter events (defined above) were separated. The simulations were made for the LEAP, HE, UHE and an additional medium energy (ME) collimator. The simulations were also separated in terms of scattered photons in the object and primary photon passing through the object without interactions.

Measurements of energy spectra

A bremsstrahlung spectrum from ^{90}Y obtained in Lucite was acquired using a HP-Ge-solid-state detector. This spectrum was then used as input for the Monte Carlo simulations. The source, a droplet with approximately 0.3 cm radius in an Eppendorff tube, was placed on a 1 cm Lucite plate, directly on the detector cover and the bremsstrahlung spectrum was registered. Lucite has a density of $\rho = 1.19$ g/cm^3 and 0.98 cm is enough to stop the electrons with a maximal energy of 2.28 MeV. An efficiency correction as function of the photon energy was made by using an earlier determined efficiency curve [17]. This curve has been obtained from a point source located on the lid of the detector (Fig. 2.4).

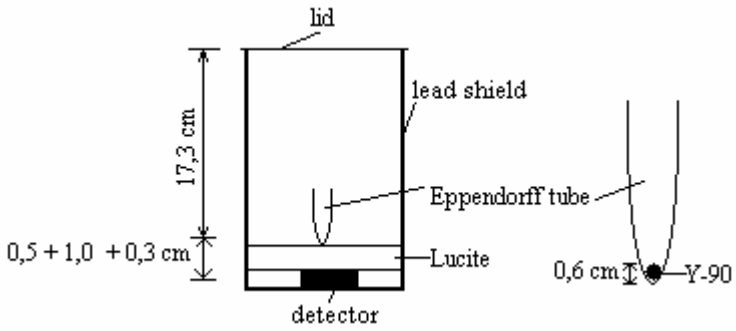

Figure 2.4 - The geometry of the HP-Ge detector.

The distance between the active volume of the detector and the detector cover is approximately 0.5 cm, the Lucite plate is 1 cm and the centre of the source, which is assumed to be a point source, is at a position 0,3 cm above the cover. This is a approximation but necessary in order to use existing efficiency curve and curve fit program. The correction factor is then determined as follows:

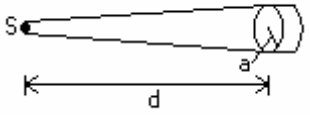

The fraction of photons impinging onto the detector is assumed to be equal to $\frac{\Omega}{4\pi}$ where Ω represents the solid angle subtended by the detector at the source position. The absolute efficiency ε_{abs} is then determined by $\varepsilon_{abs} = \varepsilon_{int} \cdot \frac{\Omega}{4\pi}$ where ε_{int} define the absolute and intrinsic efficiency, respectively.

$$\frac{\Omega}{4\pi} = \frac{1}{2}\left(1 - \frac{d}{\sqrt{d^2 + a^2}}\right)$$

$$\Omega_1 = 2\pi\left(1 - \frac{d_1}{\sqrt{d_1^2 + a^2}}\right)$$

$$\Omega_2 = 2\pi\left(1 - \frac{d_2}{\sqrt{d_2^2 + a^2}}\right)$$

$$\varepsilon_{abs.,1} = \varepsilon_{int.} \cdot \frac{\Omega_1}{4\pi} \qquad \varepsilon_{abs.,2} = \varepsilon_{int} \cdot \frac{\Omega_2}{4\pi}$$

$$\frac{\varepsilon_{abs.,1}}{\varepsilon_{abs.,2}} = \frac{\Omega_1}{\Omega_2} \Rightarrow \varepsilon_{abs.,1} = \varepsilon_{abs.,2} \cdot \frac{\Omega_1}{\Omega_2}$$

The following terms are used in the above equations:
a = 2.45 cm is the radius of the detector,
d_1 = 1.8 cm is the distance between the detector and the centre of the source and
d_2 = 6.4 cm is the distance between the detector and the centre of the source in the efficiency curve.

The resultant correction factor, $p = \frac{\Omega_1}{\Omega_2} = 6.172$. The measured value of the efficiency is, thus, multiplied by the factor p in order to get the efficiency close to the detector. The efficiency curve is based on discrete measurements. A value of the efficiency as function of the photon energy was obtained by fitting a function to the data points.

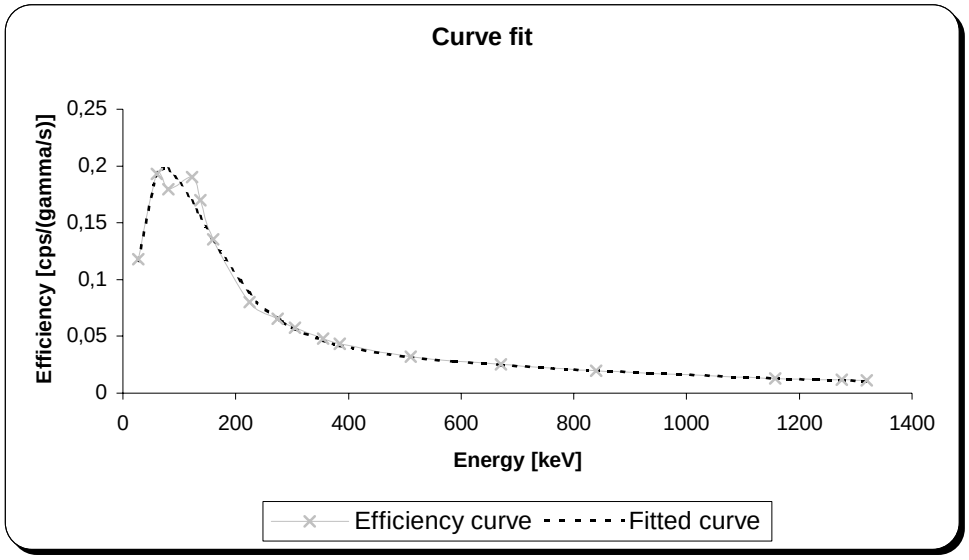

Figure 2.1 - Efficiency curve [17] and fitted curve.

The equation for curve fit in this work is as follow:

$$Eff = A_1 \cdot e^{(-E \cdot a1)} + A_2 \cdot e^{(-E \cdot a2)} + A_3 \cdot e^{(-E \cdot a3)}$$

where A_1, A_2, A_3, a_1, a_2 and a_3 are constants and E is the discrete photon energy used in the calibration measurements. The maximum deviation between the two curves were found to be 12.4% and at the 122 keV energy. The fitted curve was used for efficiency correction of the bremsstrahlung pulse-height distributions that was acquired with the HP-Ge detector.

Bremsstrahlung pulse-height distributions were also acquired using the scintillation camera and for different collimators. The energy signals were collected with an external multi-channel analyser (ACCUSPEC1) using no pulse-height amplification. The multi-channel analyser was energy-calibrated with ^{133}Ba (356 keV) and ^{137}Cs (662 keV) while ^{241}Am, ^{57}Co and ^{22}Na were used to verify the calibration. The phantom was placed as close as to the collimator as possible in order to achieve the best spatial resolution.

Evaluation of data

Region-of-interests (ROI) were defined in the acquired images using the image processing software Osiris (University Hospital of Geneva) and data was then exported to an Excel-file. The ROI's were drawn in such a way that it covered the sphere in the image with best resolution. The reason why a small ROI were defined is that only primary bremsstrahlung photons that pass through the holes should be counted but as few penetrated or scattered photon as possible. The sensitivity [cps/MBq] was determined as measured cps in the ROI divided by the known activity administered in the sphere. Decay correction was made for each image according to the formula:

$$A_{(t)} = A_{(0)} \cdot e^{-\frac{\ln 2}{T_{½}} \cdot t}$$

where $A_{(t)}$ is the activity at the time the image was acquired, $A_{(0)}$ is the activity at $t = 0$ and $T_{½}$ is the half-life of the radioisotope (64 h). To determine the primary-to-total ratio it was assumed that the counts inside the ROI originated only from primary geometrical collimated photons while events outside the ROI originated from scattered photons or photons that have penetrated the septal walls.

Radial profiles

Radial profiles were determined to average out the star-artefacts that, due to septal penetration, occur in those directions where the contents of the lead are smallest. The radial profiles were calculated by determined the pixel that has the largest value and then calculate the counts distribution along the radius from this pixel. In order to correct for the fact that sampling of counts depends on the distance; the area in the different annulus that each sample points define was used to normalize the profiles.

Development of the analytical rat

In order to evaluate the properties of small-animal imaging, a relevant computer phantom of a rat was developed. This mathematical model consists of a combination of simple geometrical shapes, (cylinders, spheres and ellipses) where each primitive is described by three-dimensional Cartesian coordinates [18]. The x-axis is directed from the model right towards its left side, the y-axis from the anterior side towards the posterior side and the z-axis from the tail towards the head, see Fig. 2.5. The origin of the coordinate system is placed at the centre of the horizontal cross-section at the bottom of the trunk.

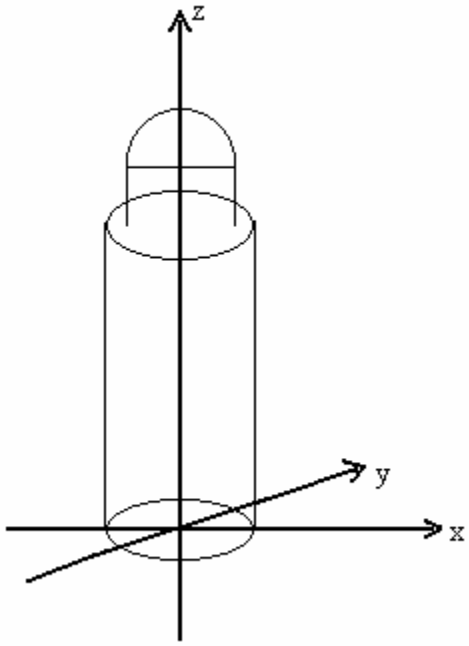

Figure 2.5 - The three-dimensional coordinate system for the mathematical model of a rat.

The mathematical expression for an ellipsoid and a cylinder are:

$$\left(\frac{x-x_0}{x_1}\right)^2+\left(\frac{y-y_0}{y_1}\right)^2+\left(\frac{z-z_0}{z_1}\right)^2\le 1 \qquad z_{\min}\le z\le z_{\max}$$

and

$$\left(\frac{x-x_0}{x_1}\right)^2+\left(\frac{y-y_0}{y_1}\right)^2\le 1 \qquad z_{\min}\le z\le z_{\max}$$

where: - x_0, y_0 and z_0 describes the displacement in proportion to x, y and z
- x_1, y_1 and z_1 determine the radii of the ellipsoid.

For example the mathematical expression for the liver is:

$$\left(\frac{x}{x_1}\right)^2+\left(\frac{y-y_0}{y_1}\right)^2+\left(\frac{z-z_0}{z_1}\right)^2\le 1$$

where $y_0=-1{,}0$, $z_0=5{,}5$, $x_1=2{,}0$, $y_1=1{,}4$, $z_1=1{,}8$

A voxel-based version was created using IDL programming language and 128 slices of 128x128 byte images were obtained. Each voxel-value defines a code that identifies which organ the voxel belongs to. From this information, both activity and density images can be obtained. The pixel size in the x- and y-direction of the phantom was set to 0.47 mm and the slice thickness was 1.25 mm.

Table 3.2
The organs in the rat model and its organ weight and the relative activity per voxel.

Organ	Weights	Relative activity per voxel
Heart	0.829	1
Kidneys	1.96	1
Liver	10.48	1
Lungs	2.00	1
Spine	5.06	1
Spleen	0.47	1
Testes	1.77	1
Thyroid	0.01	1
Remainder of body	291.0	1
Total body	313.77	1

Same size was used for the pairs of lungs, kidney, testes and thyroid glands.

All Monte Carlo simulations were based on this voxelized rat model. The matrix size of the simulated images was 128x128 and the pixel size was 1.5 mm. Note that the activity distribution only has been defined for display purposes and does not compare to any distribution of an antibody.

Results and discussions

Measurements

Figure 3.1 shows the bremsstrahlung spectra registered with an HP-Ge detector, while Figure 3.2 shows the bremsstrahlung spectra registered with the scintillation camera.

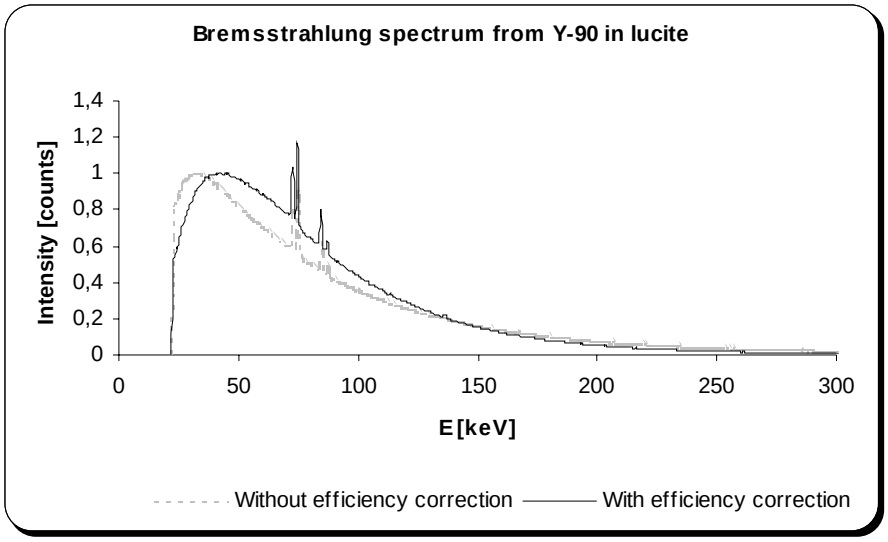

Figure 3.1 - Bremsstrahlung spectra registered with an HP-Ge detector.

The maximum energy of the bremsstrahlung spectrum reaches 2.28 MeV, but for display purposes, Figure 3.1 and 3.2 only shows the energy channels up to 300 keV. Above 300 keV, the intensity slowly continues to decrease. The peaks overlaying the bremsstrahlung spectrum around 73 keV, 75 keV, 84 keV and 85 keV originate from characteristic X-ray photon emission from the lead. The theoretical values for the most intensive characteristic X-ray photons from Pb are 74.9 keV, 72.8 keV, 84.9 keV and 84.4 keV with intensities 46.2%, 27.7%, 10.70% and 5.58%, respectively [1]. These characteristic X-ray peaks does not origin from the slowing-down of the electron and was therefore removed in the spectrum input files used in the simulations.

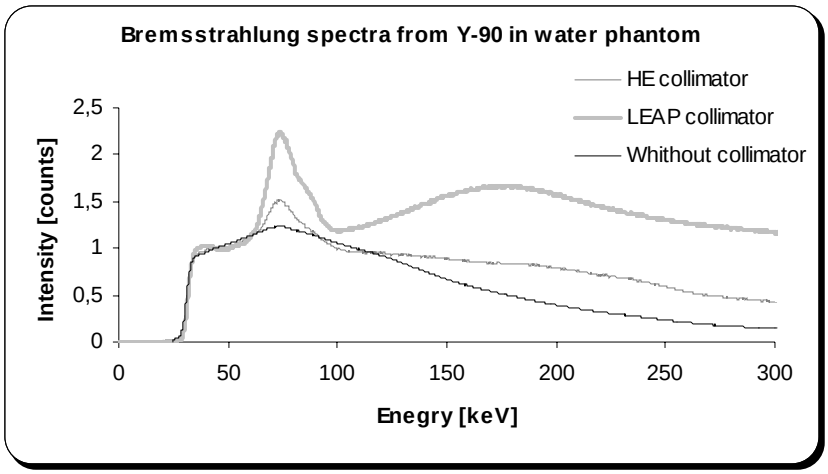

Figure 3.2 - Bremsstrahlung spectra registered with the gamma camera.

Figure 3.2 shows measured bremsstrahlung spectra using the scintillation camera with and without collimators. The curves in Figure 3.2 have been normalized to the number of counts in the 44 keV energy channel. The peak at 75 keV include counts from all of characteristic x-ray photons since it is not possible to resolve the different energies due to the limited energy resolution of the NaI(Tl) crystal. The hump around 180 keV originated from photons that have penetrated the septum. This hump is higher for the LEAP collimator than for the HE collimator. The measured sensitivity (cps/MBq) in water and air for the different collimators and the 15% energy window centred at different energies are presented in Figure 3.3. The unit of energy on the x-axis is presented in two different ways: the energy window width in keV and the window width in % centred at different energy in keV.

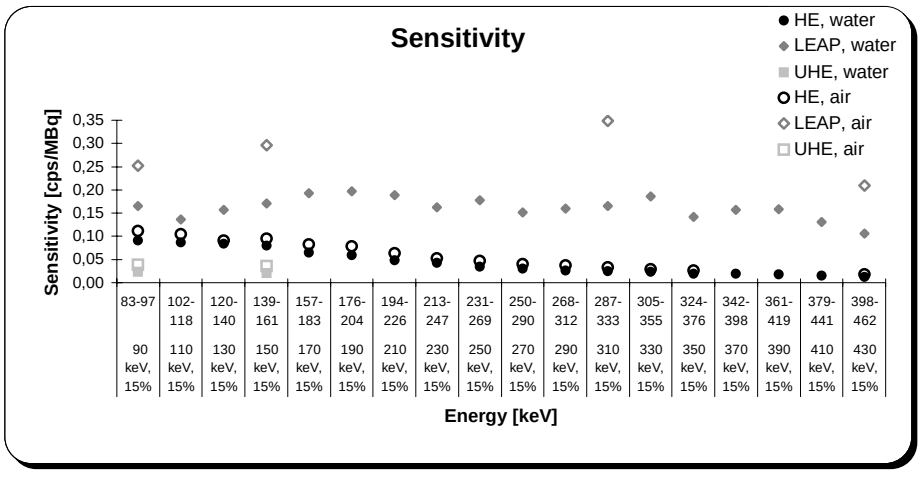

Figure 3.3 - Comparison of sensitivity in water and air for three different collimators.

A 15% energy window corresponds to a width ranging from 14 keV to 64 keV when the base line is from 90 keV to 430 keV. An increase in sensitivity is to be expected with increasing width of the energy window, but the results indicate that also the intensity of bremsstrahlung when measured in air has a significant contribution to the spectrum. The sensitivity curve for

LEAP and HE collimators show similarities with the bremsstrahlung spectrum for the same collimator, where the intensity decreases with increasing energy. The sensitivity, for a specific energy window, reaches its maximum for the LEAP collimator and is higher in the air case than in the water case for all three collimators. The sensitivity from the measurements in air may have been influenced by the β-particles from ^{90}Y that have a maximum range of about 10 meters in air - a range much larger distance than the source-to-crystal distance. The difference in sensitivity between air and water for the LEAP collimator is larger than for the HE and the UHE collimators.

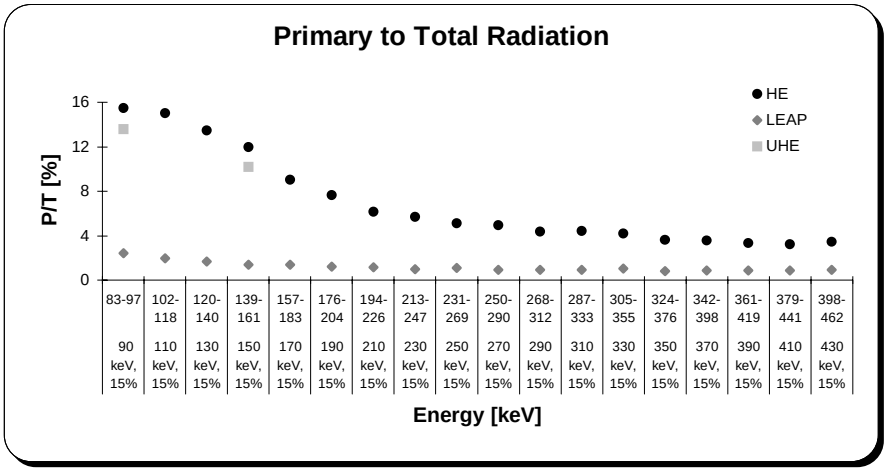

Figure 3.4 - Comparison of primary to total radiation in the water phantom for three different collimators.

Figure 3.4 shows the measured primary-to-total radiation ratio in water phantom for the three collimators. The ratio reaches is maximum at low photon energies and then decrease slowly with increasing energy. This effect is not so evident for the LEAP collimator. When comparing the three collimators, the HE collimator shows the highest primary-to-total ratio. Figure 3.5 shows the sensitivity for the water phantom case and the HE collimator when using different energy window widths but each centred at the 170 keV.

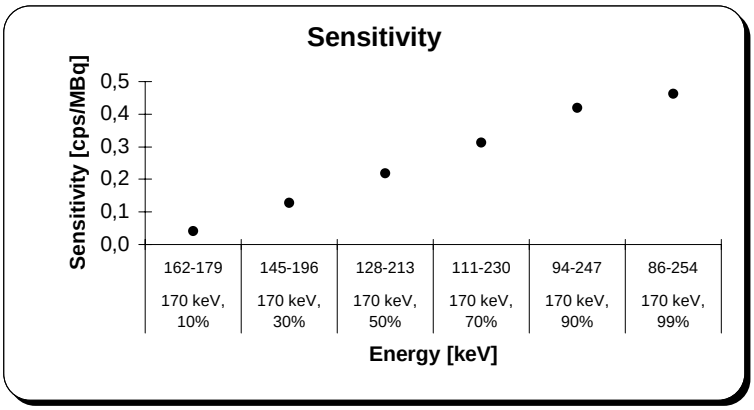

Figure 3.5 – Measured sensitivity for the water phantom case with the HE collimator.

The choice of the 170 keV energy base line for which the energy window is centred has been made in order to avoid the contribution from the lead x-rays that otherwise could spill into the window that has the maximum width (99%). The sensitivity increases as function of the energy window width as should be expected. This result is in agreement with previous reported results [9], [10], [11] and [12].

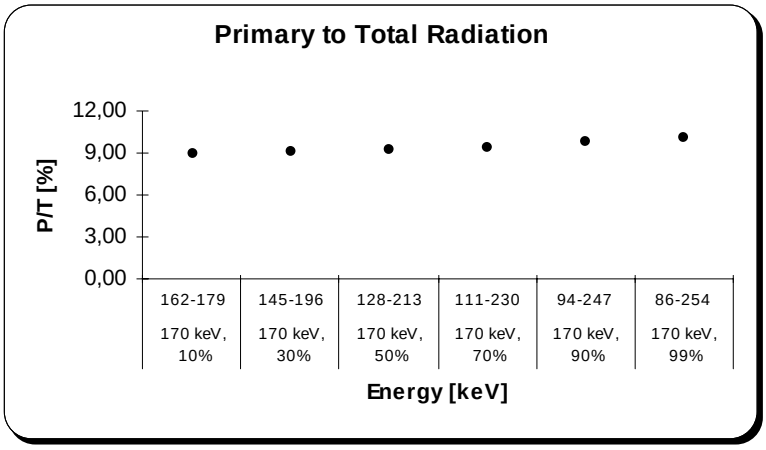

Figure 3.6 - Primary-to-total ratio when using a water phantom with HE collimator.

Figure 3.6 shows the primary-to-total radiation ratio as function of different energy window widths in HE collimator measurements. The primary-to-total ratio was here found to be almost constant and independent of the energy-window width. The ratio increases only 1% between the smallest and widest energy window.

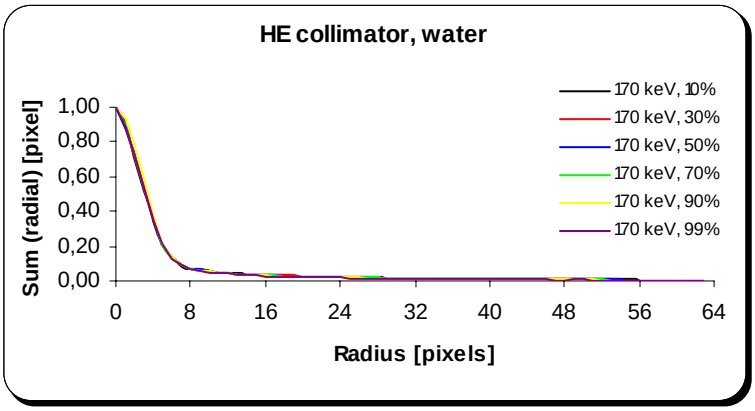

Figure 3.7 - Radial profiles as function of different energy window widths centred at 170 keV. The maximum value for each profile is normalized to 1.

Figure 3.7 shows the calculated radial count profiles of the source as function of different energy window widths centred at 170 keV. The different radial profiles were found to be very similar both close to the source and also for larges radius.

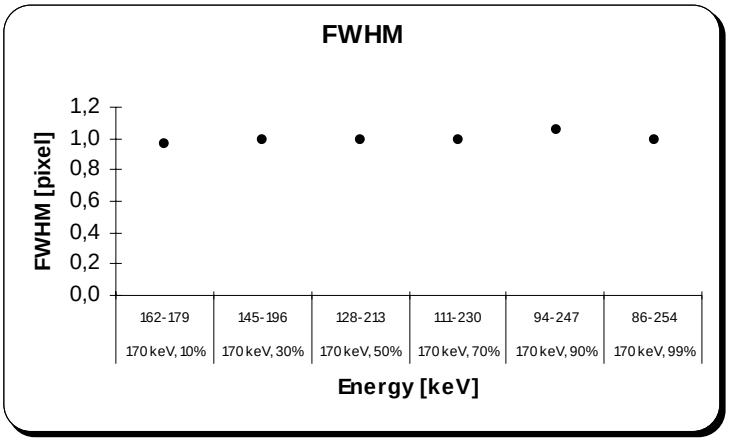

Figure 3.8 - Full-width at Half-Maximum (FWHM) normalized to the widest energy window (99%) centred at 170 keV.

From the profiles, the FWHM was determined and it was found that the FWHM did not varied significantly for the examined energy windows. This is shown in Figure 3.8.

Since the HE collimator is optimised for imaging up to around 360 keV, the collimation is efficient even for the highest energies in the broadest window. The fact that the sensitivity is highest for the widest energy window (Figure 3.5) and the primary-to-total ratio is nearly constant (Figure 3.6) implicates that a good image quality can be achieved when using the widest energy window (99%). Hence, the sensitivity was compared for the same energy window width at 99% centred at three different energies (Figure 3.9).

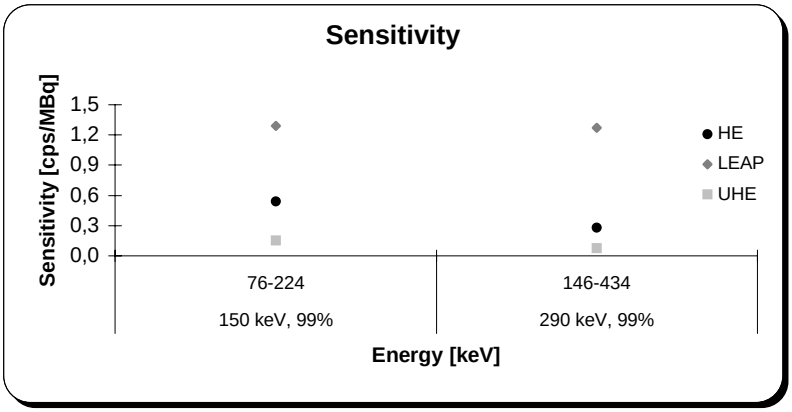

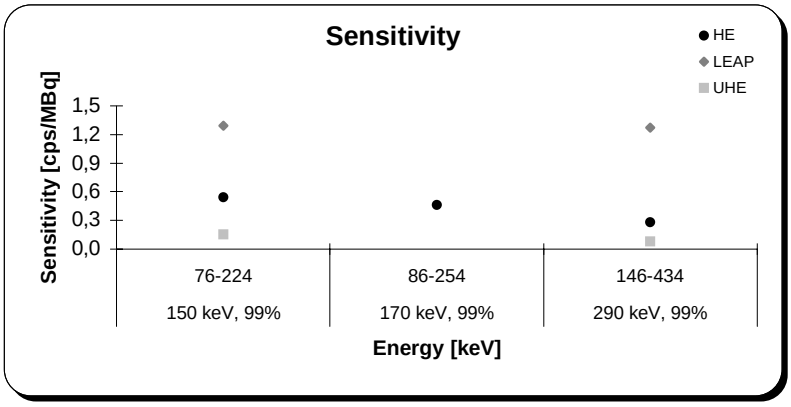

Figure 3.9 - Comparison of the system sensitivity for
the widest energy window centred at different energies.

Figure 3.9 shows that the sensitivity will decrease with increasing energy using the same collimator. The difference in sensitivity between the energy windows that were centred at 150 keV and those windows centred at around 170 keV is probably because of the additional counts from the characteristic X-rays is detected in the energy window 76-224 keV. Figure 3.9 also shows, as discussed previously, that the LEAP collimator provides the highest sensitivity. Figure 3.10 shows the primary-to-total ratio for the widest energy window (99%) centred at three different energy windows and three different collimators.

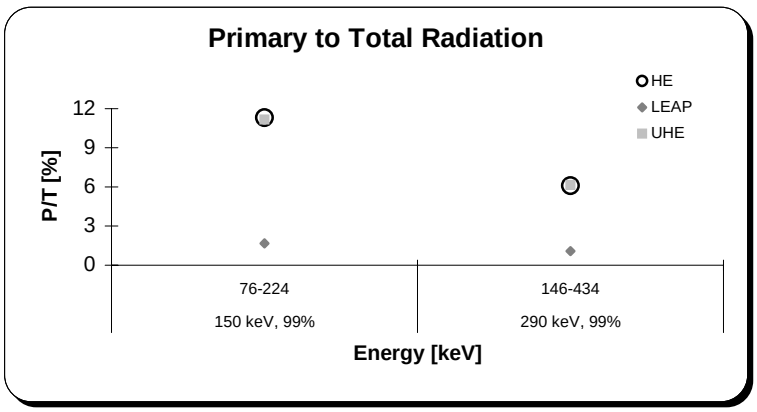

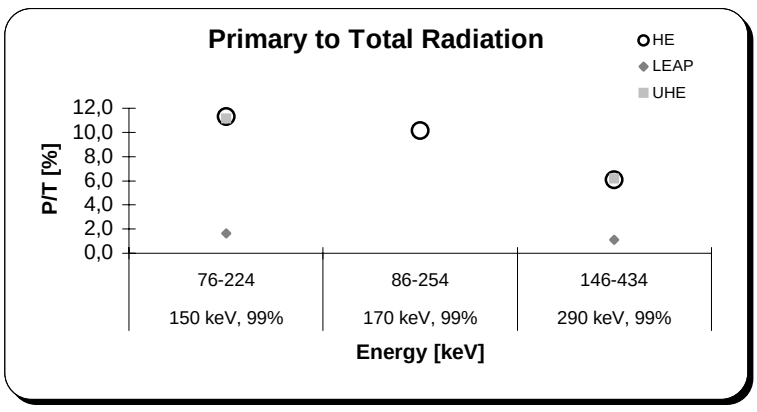

Figure 3.10 - Comparison of the primary-to-total ratio
for the widest energy window centred at different energies.

The primary-to-total ratio decreases with increasing energy for the same energy window width and the same collimator. The explanation for this can here be that for higher photon energies which lead to a larger fraction of the photons that may penetrate the septum. The number of registered counts in the whole image area therefore increases as compared to the counts in the ROI area. When comparing the primary-to-total ratio between the HE and the UHE collimators, no major difference is found. The sensitivity between the two collimators is, however, found to be more than a factor of three higher for the HE collimator.

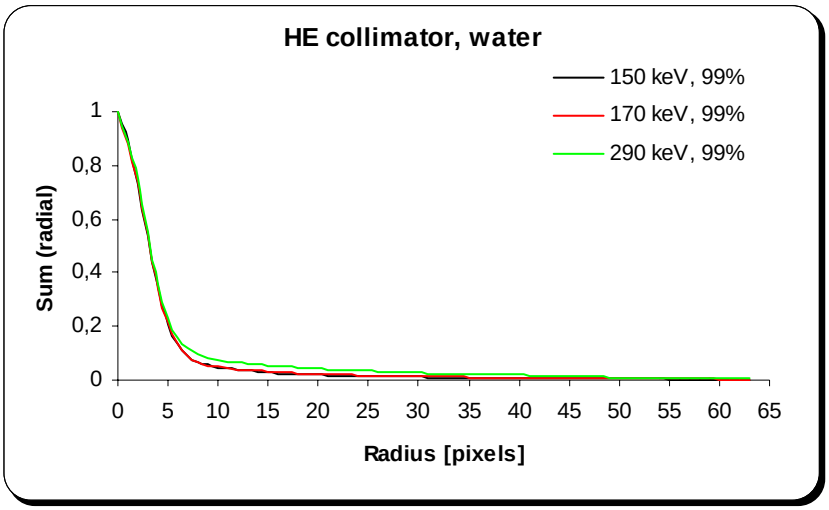

Figure 3.11 - Radial profiles for the widest energy window width centred at different energies.

The corresponding images for the profiles, shown in Figure 3.11, are shown below.

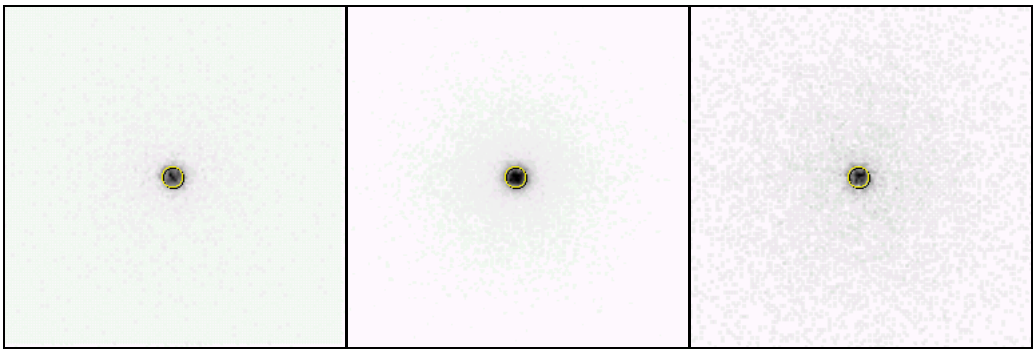

Figure 3.12 - The left image (A) shows an acquisition using the energy 150 keV energy window (99%). The total counts are here in the order of 10^4. The middle image (B) shows a similar acquisition for the 170 keV energy window (99%). Total count for this image is $5*10^4$ counts. Right image shows the acquired data for the 290 keV energy

Image C in Figure 3.12 shows, as also the profile in Figure 3.11, that the primary-to-scatter ratio is lower than in both image A and B.

Monte Carlo simulations

Pulse-height distribution from bremsstrahlung photons

Figure 3.13 shows simulated pulse-height distributions from the scintillation camera using the three collimators plus the addition medium-energy collimator (ME). It is evident that a large fraction of the events in the distribution when using the LEAP collimator originates from photons that have penetrated the septal walls. It can also be seen that the amount of counts in the low-energy region where imaging occur is reduced.

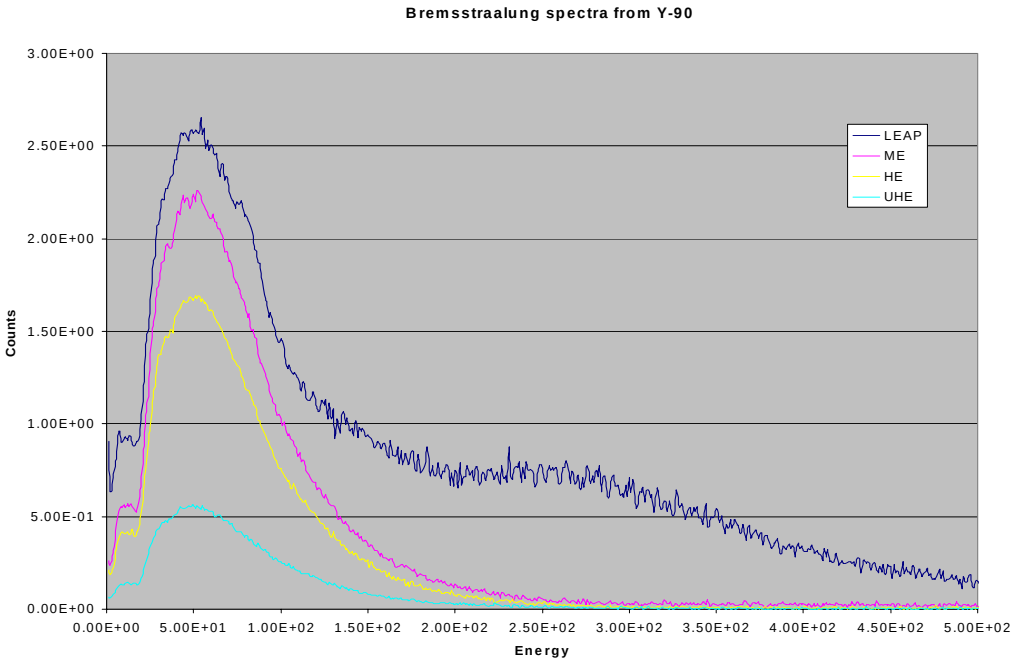

Figure 3.13 – Simulated energy spectrum using the ^{90}Y for the LEAP, HE, UHE and the additional ME collimators.

Total images

Figure 3.14 shows images including all events. The difference in sensitivity between the windows is seen as a different grey-level.

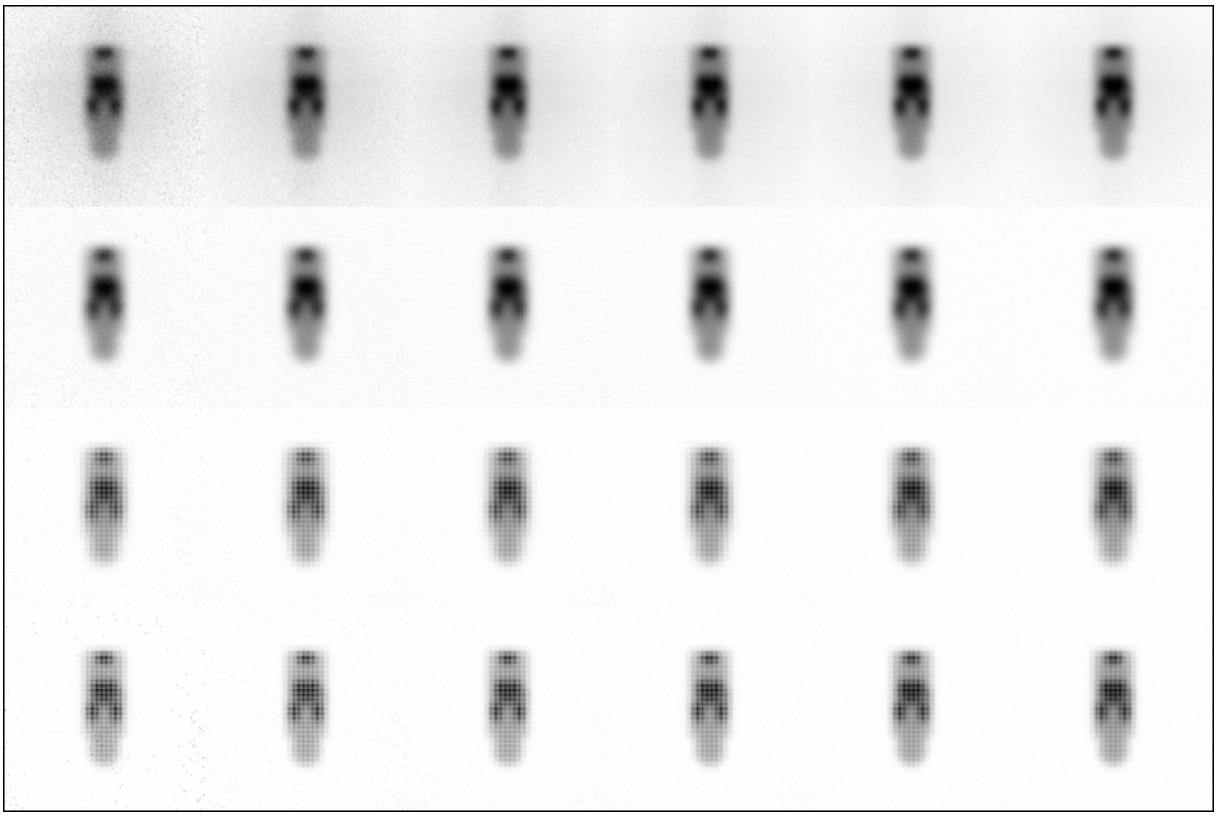

Figure 3.14 – Images showing all events resulting from photons passing the collimator. The rows are for LEAP, ME, HE and UHE collimators, respectively, starting from the top. The columns show the images for the different energy windows starting from 162-179 keV.

In Table 3.1 is shown the fraction primary-to-total for the simulation of the voxelized rat. It can be seen that the scatter part is relatively small due to the size of the rat phantom.

TABLE 3.1

	Primary / Total			
Energy Window	**LEAP**	**ME**	**HE**	**UHE**
162 - 179 keV	89%	85%	86%	85%
145 - 196 keV	88%	85%	85%	85%
128 - 213 keV	87%	83%	84%	84%
111 - 230 keV	86%	81%	82%	82%
94 - 247 keV	84%	79%	79%	79%
86 - 254 keV	83%	77%	78%	78%

The lowest values are for UHE collimator and for the widest energy window. As the energy window is decreased the ratio increased meaning that fewer miss-positioned events are registered. However, this is at the expense of a lower sensitivity (cps/MBq). The table does not indicate how much of the primary events that come from penetration and scatter in the collimator and how much that comes from geometrical collimated events.

Images of photons scatter in the object

Scatter in the phantom degrades the contrast and makes quantification of the activity difficult and non-linear. The scatter is caused by the poor energy resolution of NaI(Tl) and the use of a relatively large energy window. Simulations were therefore made for the three different cases (geometrical, penetration and scatter) by only allowing events scattered in the rat phantom. Thus, no primary photons are allowed to contribute to the formation of the images.

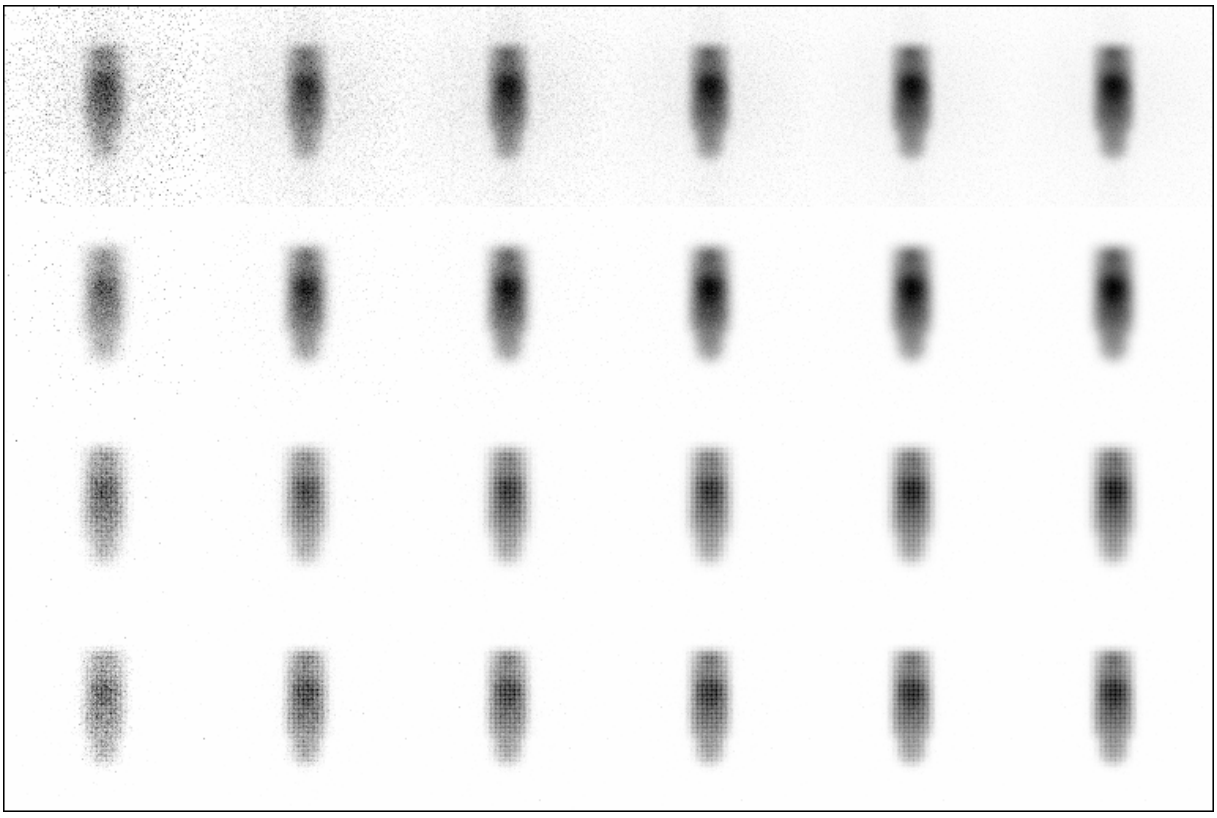

Figure 3.15 – Images showing only the events that have scattered in the rat phantom. The rows are for LEAP, ME, HE and UHE collimators, respectively, starting from the top. The columns show the images for the different energy windows starting from keV.

Contribution from geometrical collimated photons

TABLE 3.2

	Geometrical collimated primary photons			
Energy Window	**LEAP**	**ME**	**HE**	**UHE**
162 - 179 keV	30%	70%	76%	76%
145 - 196 keV	31%	71%	77%	76%
128 - 213 keV	33%	71%	76%	75%
111 - 230 keV	36%	71%	75%	75%
94 - 247 keV	38%	71%	74%	73%
86 - 254 keV	40%	70%	72%	72%

It is clear from Table 3.2 that penetration is a significant problem for LEAP making this collimator less useful for imaging. However, even for the other collimators the penetration effect also is significant. For the HE and UHE collimators, the fraction of geometrical

collimated photons is about 75% +- 5%. For the ME collimator the penetration is slightly larger – the ratio is here found to be around 70% for all energy windows. The septum penetration problem might not be that large problem since most penetration events occur close to the source location. The spatial resolution may therefore not be seriously affected. In the following section, figures of simulated planar images of the voxel-version of the analytical rat are shown in an equal format. The different rows show images simulated for the four collimators (LEAP, ME, HE and UHE). The columns represent the energy windows used.

Figure 3.16 – Images showing the 'geometrical' events resulting from photons passing the collimator without interaction or penetration. The rows are for LEAP, ME, HE and UHE collimators, respectively, starting from the top. The columns show the images for the different energy windows starting from 162-179 keV.

Contribution from photons penetrating the collimators

Table 3.3 show the fraction primary photons that penetrate through one or more septal walls. The penetration fraction is about 5% or less for HE and UHE collimators and increases for the ME collimator. For LEAP the data shows that roughly 40-50% of the registered primary photons have gone through a wall or part of it.

TABLE 3.3

Energy Window	Penetrating primary photons			
	LEAP	ME	HE	UHE
162 - 179 keV	44%	11%	6%	7%
145 - 196 keV	43%	10%	6%	7%
128 - 213 keV	40%	8%	5%	6%
111 - 230 keV	37%	7%	4%	6%
94 - 247 keV	33%	6%	3%	4%
86 - 254 keV	32%	5%	3%	4%

It can be seen from the Table that the fraction is largest for the smallest energy window in all cases. The penetration problem decreases as the photon energy decrease and at the same time the number of photons increases at lower energies. The penetration for LEAP will most likely produce a reduction in spatial resolution and from the magnitude of the penetration LEAP is not a good choice. The fraction penetrations are about twice between the ME and HE but the on the average better spatial resolution for the ME collimator this is probably a better choice. The UHE collimator shows the smallest penetration fraction, which is expected.

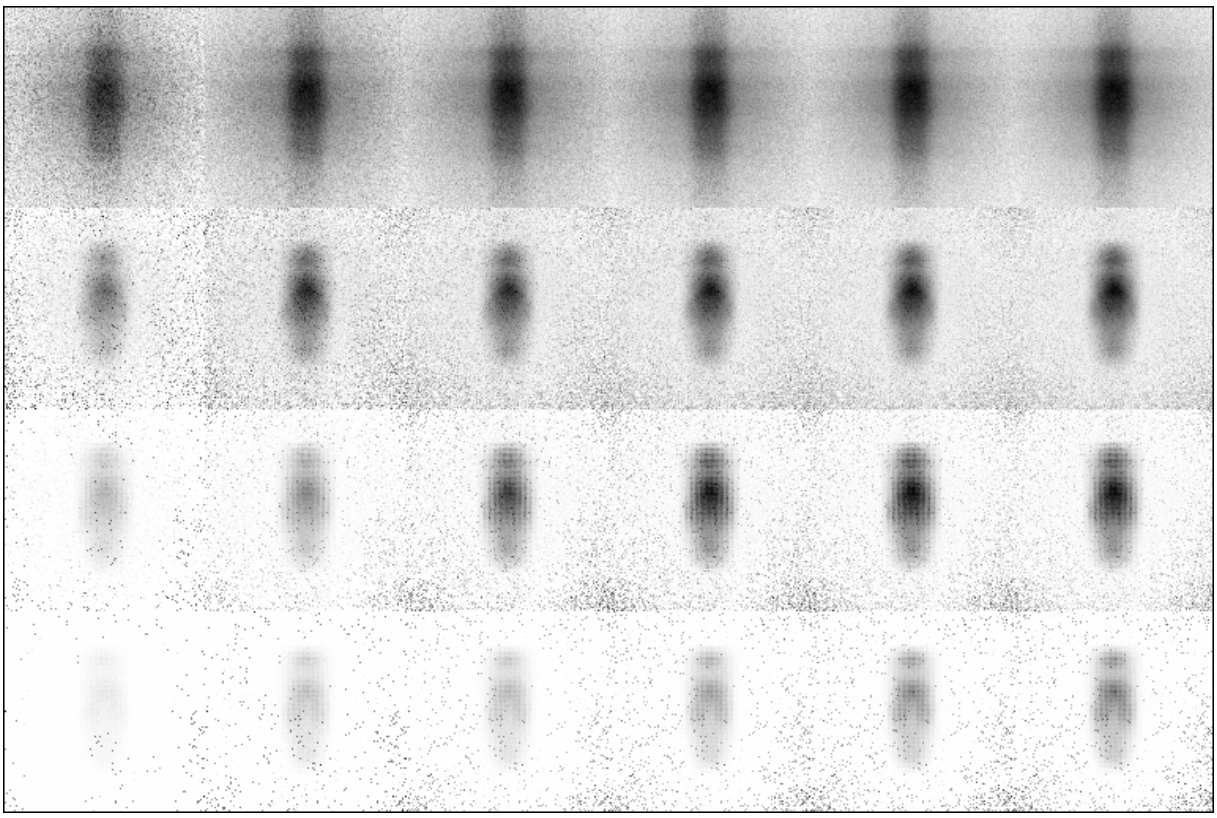

Figure 3.17 – Images showing the 'penetrating' events resulting from photons passing the collimator by penetration only. The rows are for LEAP, ME, HE and UHE collimators, respectively, starting from the top. The columns show the images for the different energy windows starting from 162-179 keV.

Contribution from primary photons scattered in the collimator

Table 3.4 show the fraction primary photons that have been scattered in the collimator.

TABLE 3.4

	Fraction primary photons scattered in the collimator			
Energy Window	**LEAP**	**ME**	**HE**	**UHE**
162 - 179 keV	15%	5%	3%	2%
145 - 196 keV	15%	5%	3%	2%
128 - 213 keV	14%	4%	2%	2%
111 - 230 keV	13%	3%	2%	2%
94 - 247 keV	12%	3%	2%	1%
86 - 254 keV	12%	3%	2%	1%

Figure 3.18 shows the distribution in the images coming from primary photons scattered in the collimator. The primary photons that undergo scatter (and a possible penetration) in the collimator are quite few for the ME, HE and UHE and around 17% percent for the LEAP collimator. Many of these scattered photons still have relatively high energies, which means they still can penetrate septa in the LEAP collimator

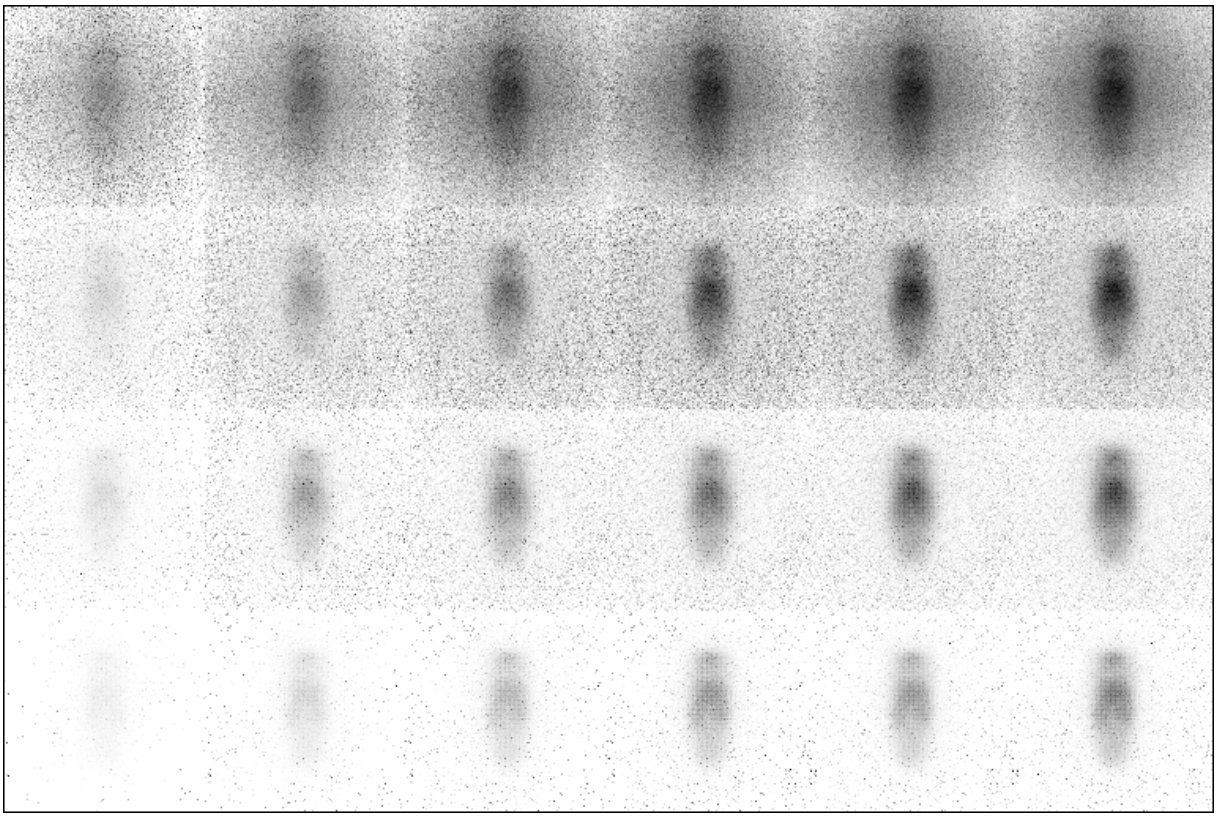

Figure 3.18 – Images showing the 'collimator scattered' events resulting from photons passing the collimator by Compton scattering in the lead septa. The rows are for LEAP, ME, HE and UHE collimators, respectively, starting from the top. The columns show the images for the different energy windows starting from 162-179 keV.

Conclusions

The measurements indicate that the widest window (99%) should be used since the primary-to-total ratio remains constant while the sensitivity increases with the width of the energy window. The centre of the energy window should be placed at 170 keV although both the sensitivity and primary-to-total ratio is higher at 150 keV. The reason for this is the assumption that the events from the characteristic radiation below 85 keV. The results from the Monte Carlo calculation indicate that this method can be useful for evaluation of imaging parameter because of its capability to differentiate the events into separate components. Important parameters, such as the primary-to-total ratio, can then be determined and serve as an aid when developing correction methods for scatter, attenuation and septal penetration.

Future work could be continued with investigations of several tumours at different sizes in the same phantom. As small animals are imaged another collimator, the pinhole collimator, ought to be investigated. In order to achieve gamma camera parameters in clinical applications a more realistic model, like a human body phantom, should be used.

References

1. Table of Isotopes, Eight Edition, Richard B Firestone and Virginia S Shirley
2. Martin J Berger, J Nucl Med, 7-24, Vol. 12, (1971)
3. Lars Hallstadius, Sven Hertzman, Joniserande strålnings växelverkan med materia, Radiofysiska Institutionen 1984, (pp. 54 and 68-74)
4. Kenneth S Krane, Introductory Nuclear Physics, (pp.194, 196)
5. J A Sörenson and M E Phelps; Physics in Nuclear Medicine (Grune and Stratton, New York, 1998)
6. Glenn F Knoll, Radiation Detection and Measurements, Second Edition, (pp.33-332)
7. M Ljungberg, S-E Strand and M A King; Monte Carlo Calculations in Nuclear Medicine (pp. 63-76)
8. Web; The Physics of Medical Imaging (pp.161-171)
9. Larry E Dillehay et al, Use of Bremsstrahlung Radiation to Monitor ^{90}Y Tumour and Whole Body Activities during Experimental Radioimmunotherapy in Mice, Cancer 1194; 73:945-50
10. Laurence P Clarke, Shelby J Cullom, Robin Shaw, Curt Reece, Bill C Penney, Michael A King and Martin Silbiger, Bremsstrahlung Imaging Using the Gamma Camera: Factors Affecting Attenuation, J Nucl Med 1992; 33:161-166

11. Jeffery A. Siegel, Stacy Whyte-Ellis, Louise S. Zeiger, Stanley E. Order and Paul E. Wallner, Bremsstrahlung SPECT Imaging and Volume Quantitation with ^{32}Phosphorus, Antibody, Immunoconjugates and Radiopharmaceuticals Volume7, Number 1,1994
12. Sui Shen, Gerald L DeNardo, Aina Yuan, Diane A DeNardo and Sally J DeNardo, Planar Gamma Camera Imaging and Quantitation of Yttrium-90 Bremsstrahlung, J Nucl Med 1994; 33:1381-1389
13. Sui Shen, Gerald L DeNardo and Sally J DeNardo; Quantitative Bremsstrahlung Imaging of Yttrium-90 Using a Wiener Filter, Med Phys 21 (9), September 1994
14. Hand book for the DIACAM Scintillation Camera System
15. Ljungberg M, Strand S-E. A Monte Carlo Program Simulating Scintillation Camera Imaging. Comp Meth Progr Biomed 1989; 29:257-272.
16. DeVries DJ, Moore SC, Zimmerman RE, Friedland B, Lanza RC. Development and Validation of a Monte Carlo Simulation of Photon Transport in an Anger Camera. IEEE Trans Med Imag 1990; 4:430-438.
17. Personal communication: Gustav Grafström and Per Roos.
18. ICRU Report 48, Phantoms and Computational models in therapy, diagnose and protection.